



# Radial viscous fingering of hot asthenosphere within the Icelandic plume beneath the North Atlantic Ocean



C.M. Schoonman<sup>a</sup>, N.J. White<sup>a,\*</sup>, D. Pritchard<sup>b</sup>

<sup>a</sup> Bullard Laboratories, Department of Earth Sciences, University of Cambridge, Madingley Rise, Madingley Road, Cambridge, CB3 0EZ, UK

<sup>b</sup> Department of Mathematics and Statistics, University of Strathclyde, Livingstone Tower, 26 Richmond Street, Glasgow, G1 1XH, Scotland, UK

## ARTICLE INFO

### Article history:

Received 21 November 2016

Received in revised form 28 March 2017

Accepted 29 March 2017

Available online 13 April 2017

Editor: P. Shearer

### Keywords:

viscous fingering

Iceland

mantle plumes

dynamic topography

## ABSTRACT

The Icelandic mantle plume has had a significant influence on the geologic and oceanographic evolution of the North Atlantic Ocean during Cenozoic times. Full-waveform tomographic imaging of this region shows that the planform of this plume has a complex irregular shape with significant shear wave velocity anomalies lying beneath the lithospheric plates at a depth of 100–200 km. The distribution of these anomalies suggests that about five horizontal fingers extend radially beneath the fringing continental margins. The best-imaged fingers lie beneath the British Isles and beneath western Norway where significant departures from crustal isostatic equilibrium have been measured. Here, we propose that these radial fingers are generated by a phenomenon known as the Saffman–Taylor instability. Experimental and theoretical analyses show that fingering occurs when a less viscous fluid is injected into a more viscous fluid. In radial, miscible fingering, the wavelength and number of fingers are controlled by the mobility ratio (i.e. the ratio of viscosities), by the Péclet number (i.e. the ratio of advective and diffusive transport rates), and by the thickness of the horizontal layer into which fluid is injected. We combine shear wave velocity estimates with residual depth measurements around the Atlantic margins to estimate the planform distribution of temperature and viscosity within a horizontal asthenospheric layer beneath the lithospheric plate. Our estimates suggest that the mobility ratio is at least 20–50, that the Péclet number is  $O(10^4)$ , and that the asthenospheric channel is  $100 \pm 20$  km thick. The existence and planform of fingering is consistent with experimental observations and with theoretical arguments. A useful rule of thumb is that the wavelength of fingering is  $5 \pm 1$  times the thickness of the horizontal layer. Our proposal has been further tested by examining plumes of different vigor and planform (e.g. Hawaii, Cape Verde, Yellowstone). Our results support the notion that dynamic topography of the Earth's surface can be influenced by fast, irregular horizontal flow within thin, but rapidly evolving, asthenospheric fingers.

© 2017 Elsevier B.V. All rights reserved.

## 1. Introduction

It is generally agreed that a substantial convective upwelling or plume centered beneath Iceland has had a significant effect on the stratigraphic evolution of the North Atlantic Ocean (White and McKenzie, 1989; Jones et al., 2012). This plume developed during Early Cenozoic times and its inception is usually linked with the appearance of basaltic magmatism at 64 Ma. It is bisected by a mid-oceanic ridge which provides a helpful window into the detailed temporal evolution of this globally significant feature (Parnell-Turner et al., 2014). Fluctuations in plume activity over the last 50 Ma are recorded in the pattern of diachronous V-shaped ridges that are imaged in the oceanic basins on either side of the

Reykjanes Ridge. During the Neogene period, regional bathymetric changes associated with these fluctuations appear to have moderated overflow of Northern Component Water, the ancient precursor of North Atlantic Deep Water (Poore et al., 2011).

The present-day planform of the Icelandic plume is determined from a combination of three different sets of observations (Fig. 1). The simplest and most striking manifestation is the pattern of long wavelength (700–2500 km) free-air gravity anomalies. A positive anomaly of 30–50 mGal is centered on Iceland. Together, other anomalies form an irregular planform that reaches from Baffin Island to western Scandinavia, and from the Charlie-Gibbs fracture zone to Svalbard. The inference that this pattern of long wavelength anomalies is a manifestation of mantle convective upwelling is strengthened by the existence of significant residual depth anomalies throughout adjacent oceanic basins. Hoggard et al. (2017) built a database of seismic reflection and wide-angle profiles that they used to accurately calculate water-loaded depths

\* Corresponding author.

E-mail address: njw10@cam.ac.uk (N.J. White).

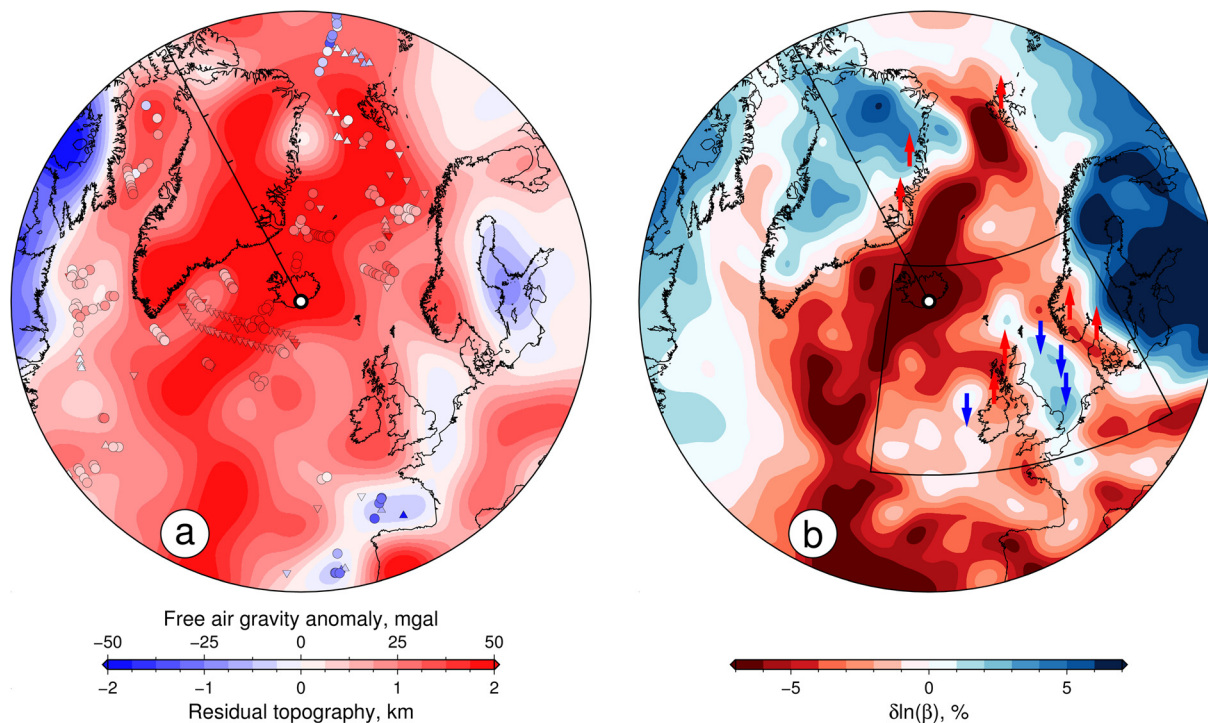


**Fig. 1. Residual topography and velocity structure.** (a) Map of residual topography of North Atlantic Ocean calculated from long wavelength (700–2500 km) free-air gravity anomalies using water-loaded admittance of  $Z = 25 \text{ mGal km}^{-1}$ . Circles = residual depth anomaly measurements on oceanic crust with both sedimentary and crustal corrections (Hoggard et al., 2017); upward-/downward-pointing triangles = upper/lower limits for residual depth anomaly measurements with sedimentary corrections only; white circle = center of Icelandic plume (Shottle et al., 2010); ticks on scale bar plotted every 500 km. Azimuthal polar projection centered on Iceland where radius = 2800 km. (b) Map of shear wave velocity anomaly,  $V_s$ , with respect to Preliminary Reference Earth Model (PREM) at depth of 150 km (Rickers et al., 2013). Red/blue arrows = loci of anomalous Neogene uplift/subsidence events (Kooi et al., 1991; Anell et al., 2009; Davis et al., 2012); box = location of Fig. 2. For interpretation of colors in this figure, reader is referred to web version of this article.

to oceanic basement as a function of plate age. In this way, residual depth anomalies are determined that build upon previous analyses (White, 1997; Marquart and Schmeling, 2004). These combined results show that oceanic crust surrounding Iceland is considerably shallower than expected (Fig. 1a). For example, residual depth anomalies of up to 2 km are recorded adjacent to Iceland. This regional shallowing dies out gradually with increasing distance from Iceland. The match between residual depth measurements and long wavelength gravity anomalies is reasonable, although a notable exception is observed north of Greenland. The relationship between the gravity field and residual depth measurements suggests that the water-loaded admittance is  $Z \sim +25 \text{ mGal km}^{-1}$ , in agreement with global studies (Crosby and McKenzie, 2009).

Finally, the presence of a mantle convective anomaly is corroborated by earthquake tomographic models which suggest that an extensive and irregular patch of low shear wave velocity lies beneath the lithospheric plates (Bijwaard and Spakman, 1999; Ritsema et al., 2011). The most striking of these studies is that of Rickers et al. (2013) who use full-waveform tomography to build a high resolution shear wave velocity model of the North Atlantic region from the surface to a depth of 1300 km (Fig. 1b). A significant negative velocity anomaly of  $>10\%$  with respect to their reference model is centered beneath Iceland, in agreement with earlier studies. One notable feature of their model is the existence of narrow, slow velocity fingers that protrude beneath the fringing continental margins. Two prominent fingers reach beneath the British Isles and western Norway. In both cases, the associated negative shear wave velocity anomalies are  $>2\%$  and sit within a  $100 \pm 20 \text{ km}$  thick horizontal layer immediately beneath the lithospheric plate (Fig. 2). Rickers et al. (2013) show that there is a reasonable match between the loci of these fingers and long wavelength gravity anomalies. Significantly, both fingers also coincide with crustal isostatic anomalies and with the general pattern of

Neogene vertical movements observed across the northwest shelf of Europe (Anell et al., 2009; Davis et al., 2012). In the southern North Sea, the fast (i.e. cooler) region between these fingers has a water-loaded subsidence anomaly of  $\sim 500 \text{ m}$  that grew in Neogene times and represents a significant departure from the expected thermal subsidence trajectory (Fig. 2b–d; Kooi et al., 1991). This region probably subsided as a result of small-scale convective downwelling between the two warm fingers.

Here, we combine these different geologic and geophysical observations to investigate the causes and consequences of radial fingering within the asthenospheric mantle. In a series of contributions pioneered by Weeraratne et al. (2003), it has been suggested that some combination of rectilinear viscous fingering instabilities, small-scale convection, and shear-driven upwelling may play a role in explaining the observed pattern of seismic velocity anomalies beneath the southern portion of the East Pacific Rise (Weeraratne et al., 2007; Harmon et al., 2011; Ballmer et al., 2013). Although there are significant geometric and mechanical differences, our analysis evidently builds upon these previous contributions and upon the analysis of Morgan et al. (2013).

Our approach is divided into three steps. First, we present the physical characteristics of the Icelandic plume, such as its size, shape and vigor. By combining the correlation between shear wave velocity anomalies and the pattern of regional Neogene epeirogeny with a global empirical relationship between shear wave velocity and temperature, we estimate how viscosity within the plume head spatially varies. Secondly, we compare these observations of plume behavior beneath Iceland and elsewhere with published laboratory experiments that investigate the development of radial miscible viscous fingering. Thirdly, the development of radial fingering is discussed using a suite of theoretical and heuristic arguments. We conclude by exploring the implication of our hypothesis for a small selection of well-known plumes.

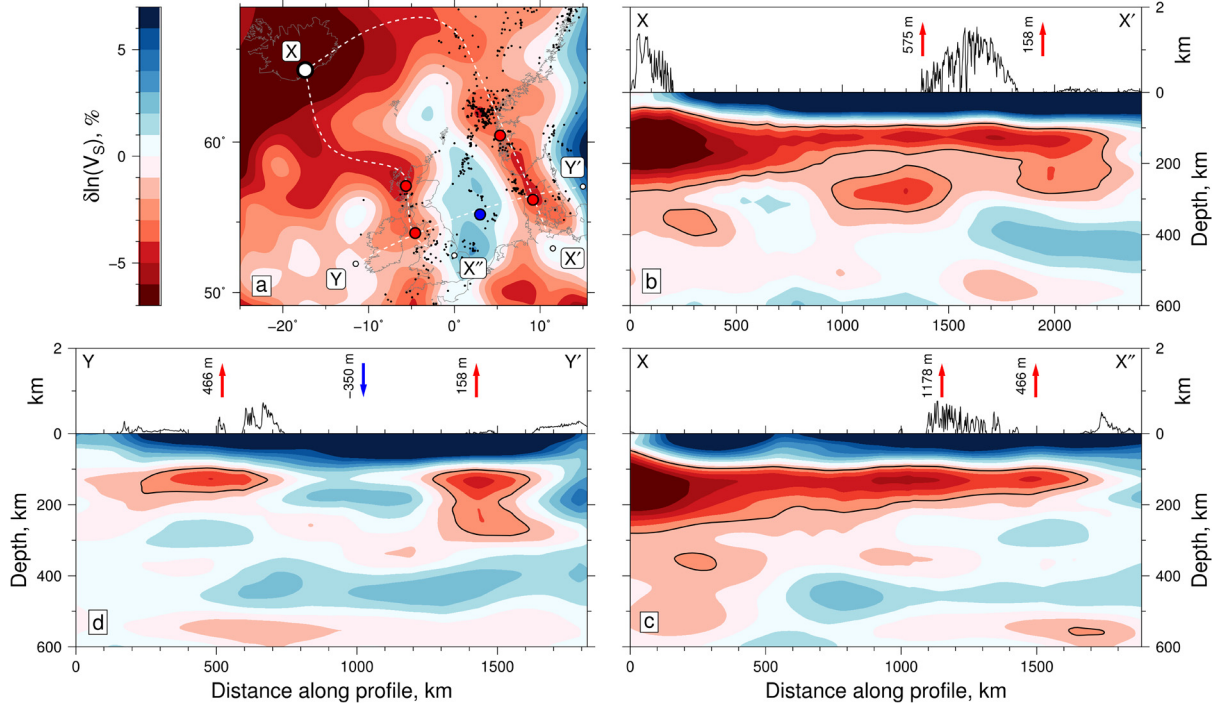


**Fig. 2. Velocity anomalies and vertical displacements.** (a) Map of northwest shelf of Europe showing shear wave velocity anomalies at depth of 150 km (Rickers et al., 2013). White circle = center of Icelandic plume (Shorttle et al., 2010); red circles = loci with positive crustal isostatic anomalies; blue circle = locus of anomalous Neogene subsidence; black circles = loci of earthquakes ( $M_b \geq 3$ ) from catalogues of British Geological Survey (<http://www.earthquakes.bgs.ac.uk>), Geological Survey of Denmark and Greenland (<http://www.geus.dk>) and University of Helsinki (<http://www.seismo.helsinki.fi>); white dashed lines labeled X-X', X-X'' and Y-Y' = 3 vertical transects through shear wave velocity model. (b) Vertical transect along X-X'. Upper panel = topography along transect; numbered red arrows = estimates of dynamic uplift calculated from crustal receiver functions (Davis et al., 2012). (c) Vertical transect along X-X''. Upper panel = topography along transect; numbered red arrows = estimates of dynamic uplift as before. (d) Vertical transect along Y-Y'. Upper panel = topography along transect; numbered red arrows = estimates of dynamic uplift as before; numbered blue arrow = estimate of water-loaded Neogene subsidence anomaly (Kooi et al., 1991; Anell et al., 2009). For interpretation of colors in this figure, reader is referred to web version of this article.

## 2. Physical characteristics of Icelandic plume

The temperature structure of the Icelandic plume can be estimated in a variety of related ways. In the North Atlantic Ocean, a mid-oceanic spreading center transects this plume and provides the most straightforward method for determining this structure. Within the region of influence, the average thickness of oceanic crust increases from 7 to 14 km and the seabed is anomalously shallow by up to 2 km (Fig. 1; White, 1997). Both of these observations are consistent with an average temperature anomaly of 150–200 °C. This value is corroborated by multi-lithologic modeling of olivine-spinel-aluminum exchange thermometric observations of basaltic samples from the Northern Volcanic Zone, adjacent to the plume conduit itself (Matthews et al., 2016). South of Iceland along the Reykjanes Ridge, Parnell-Turner et al. (2014) argue that plume temperature also fluctuates by 25–30 °C with a periodicity of up to 8 Ma over the last 50 Ma. They suggested that the Icelandic plume shrank dramatically toward the end of Eocene times and that the present-day planform of this convective upwelling was established in the last 30–40 Ma.

The present-day thermal structure of the Icelandic plume can be independently gauged by exploiting the consistent relationship between shear wave velocity anomalies and residual depth observations together with an empirically determined global relationship that relates shear wave velocity to temperature and pressure (Priestley and McKenzie, 2006). Beneath northern Britain and western Norway, Neogene vertical motions have been attributed to temperature anomalies within an asthenospheric channel (Bott and Bott, 2004). The amplitude of uplift or subsidence is related to the average excess temperature of the channel. At large distances from the plume center, it is reasonable to assume that asthenospheric

flow is predominantly horizontal. In this case, an isostatic balance shows that

$$U = \frac{b\alpha\bar{T}}{1 - \alpha T_r} \quad (1)$$

where  $U$  is surface uplift,  $b$  is the thickness of the asthenospheric layer,  $\alpha = 3.4 \times 10^{-5} \text{ } ^\circ\text{C}^{-1}$  is the thermal expansion coefficient,  $T_r = 1315 \text{ } ^\circ\text{C}$  is the ambient asthenospheric temperature, and  $\bar{T}$  is the average excess temperature across the channel (e.g. Rudge et al., 2008). Furthermore, the wavelength of asthenospheric anomalies is  $O(10^2)$  km, which is large compared to the elastic thickness of the lithosphere of the northwest European shelf. Davis et al. (2012) exploit crustal thickness measurements from receiver function analysis to show that northwest Scotland has an average anomalous elevation of  $\sim 500$  m. They suggest that this elevation is maintained by a sub-plate density anomaly, which they attribute to a layer of warm asthenosphere (Morgan et al., 2013). For example, if this layer is  $100 \pm 20$  km thick, Equation (1) yields an asthenospheric temperature anomaly of  $\bar{T} = 140_{117}^{176} \text{ } ^\circ\text{C}$ . According to Rickers et al. (2013), the shear wave velocity anomaly beneath Scotland is  $V_s = 4.23 \pm 0.10 \text{ km s}^{-1}$ .

These local values prescribe an empirical relationship between temperature, depth and shear wave velocity that can be validated against the global calibration of Priestley and McKenzie (2006) who combined a thermal parameterization of a stacked surface wave tomographic model of oceanic plates with pressure/temperature estimates from mantle nodules to calculate shear wave velocity as a function of temperature, pressure and activation process. Between 1300 °C and 1500 °C at a depth of 150 km, their parameterization can be approximated by

$$V_s = 0.187 \ln(1500 - T) + 3.533 \quad (2)$$



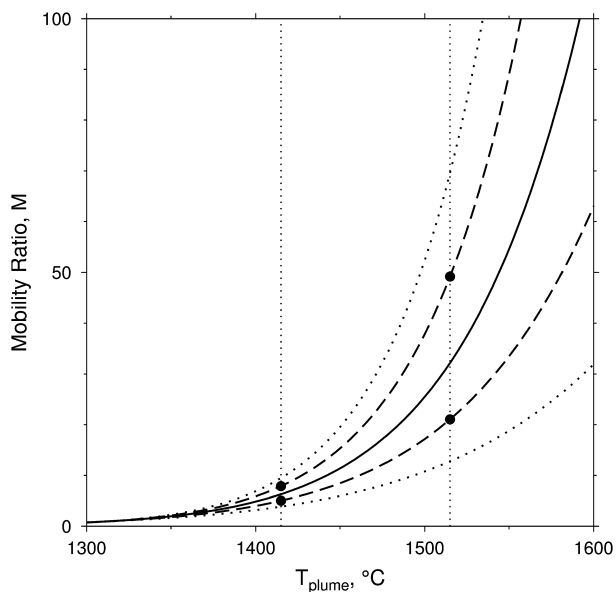


**Fig. 3. Relationship between plume temperature and viscosity.** Mobility ratio (i.e.  $\eta_r/\eta$ ) plotted as function of plume temperature for different values of activation energy. Solid/dashed lines represent  $E = 409 \pm 50 \text{ kJ mol}^{-1}$  (Priestley and McKenzie, 2006); dotted lines represent  $E = 300$  and  $500 \text{ kJ mol}^{-1}$ ; vertical dotted lines = range of plume temperatures (Parnell-Turner et al., 2014); solid circles = range of likely values of  $M$  for proximal and distal parts of Icelandic plume.

This approximation yields  $V_s \approx 4.24 \pm 0.10 \text{ km s}^{-1}$  for an asthenospheric temperature of  $1455^\circ\text{C}$ , in close agreement with Rickers et al. (2013).

This empirical relationship between shear wave velocity and temperature at a depth of 150 km can be used to construct a temperature-dependent map of viscosity within the asthenospheric channel. The viscosity contrast between plume material and the surrounding ambient mantle is given by the mobility ratio,  $M$ , where

$$M = \frac{\eta_r}{\eta}. \quad (3)$$

$\eta_r$  is the viscosity of ambient mantle and  $\eta$  is the viscosity of plume material where

$$\eta = \eta_r \exp \left\{ \frac{E}{R} \left( \frac{1}{(T + 273)} - \frac{1}{(T_r + 273)} \right) \right\}. \quad (4)$$

$E = 409 \pm 50 \text{ kJ/mol}$  is the activation energy of mantle rock,  $R = 8.3 \text{ J/mol/K}$  is the gas constant, and pressure dependence terms are neglected (Fig. 3). Our chosen range for  $E$  matches the optimal values calculated by inverse modeling (Priestley and McKenzie, 2006). For a temperature anomaly of, for example,  $200^\circ\text{C}$ , we obtain  $M = 32 \pm 15$ .

It is generally accepted that dislocation creep is probably the dominant mechanism within the asthenospheric mantle (Behn et al., 2009). If so, our assumption that  $E = 409 \pm 50 \text{ kJ/mol}$  is a reasonable lower bound. Two different sets of laboratory experiments suggest that dry dislocation creep of fine-grained olivine aggregates is consistent with  $E = 530 \pm 40 \text{ kJ/mol}$  or  $550 \pm 20 \text{ kJ/mol}$  (Hirth and Kohlstedt, 2003). Wet dislocation creep is consistent with  $E = 510 \pm 70 \text{ kJ/mol}$  or  $E = 530 \pm 30 \text{ kJ/mol}$ . Significantly, these values yield even greater mobility ratios. In contrast, analysis of different combinations of dry and wet diffusion creep experiments is consistent with activation energies as low as  $E = 375 \pm 50 \text{ kJ/mol}$  and  $E = 380 \pm 20$  or  $410 \pm 40 \text{ kJ/mol}$ , respectively. If  $E$  is as low as  $300 \text{ kJ/mol}$ , which is unlikely, values of  $M = 5\text{--}10$  are obtained (Fig. 3). As the solidus is approached, very small melt fractions affect both shear wave velocity and viscosity (e.g. McCarthy and Takei, 2011). For example, anelastic effects can cause

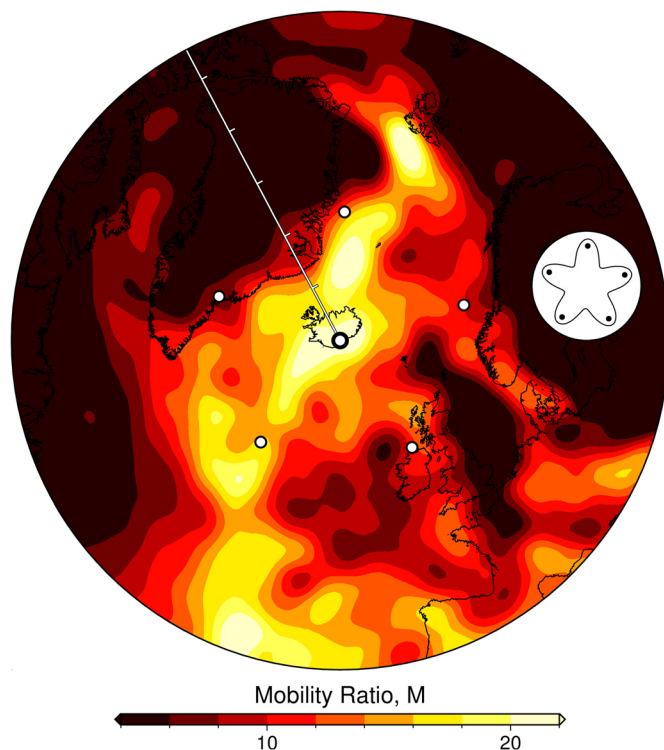


**Fig. 4. Mobility ratio beneath North Atlantic Ocean.** Map of mobility ratio,  $M$ , at 150 km depth calculated by converting shear wave velocity anomalies from Rickers et al. (2013) into  $M$  using Equations (2)–(4) with  $E = 409 \text{ kJ mol}^{-1}$  (note that reference viscosity is that of ambient oceanic asthenosphere so this calculation is not designed to be reliable within continental cratons). Large white circle = center of Icelandic plume (Shorttle et al., 2010); small white circles = loci of finger tips obtained by visually matching Equation (5) with  $n = 5$  (see inset). Azimuthal polar projection centered on Iceland where radius = 2800 km. Ticks on scale bar plotted every 500 km.

shear velocity to be reduced by  $\geq 5\%$  across the solidus for a melt fraction of 0.01 (see Fig. 4 of Holtzman, 2016). More significantly, melt fractions as low as 0.003 can cause viscosity to decrease by as much as two orders of magnitude (McCarthy and Takei, 2011). Given the absence of basaltic melting that tracks the observed fingers, the observational uncertainties for  $V_s$ , and the fact that our estimate of mobility ratio is necessarily a lower limit, these complications can be safely neglected here.

Fig. 4 shows the radial distribution of  $M$  calculated using Equations (2)–(4) at a horizontal depth of 150 km for the Icelandic plume. Within the central part of this plume,  $M \sim 24$ . Fingers that reach beneath the British Isles and western Norway have  $M = 10\text{--}15$ . Note that  $M$  is calculated with respect to the viscosity of ambient asthenosphere and its putative value beneath adjacent continental cratons should be ignored. The full-waveform inverse modeling results of Rickers et al. (2013), as well as other surface wave tomographic models, suggest that these low viscosity fingers are confined within a thin layer immediately beneath the lithospheric plates. This layer is  $100 \pm 20 \text{ km}$  thick (Fig. 2b–d). The absence of any measurable relief on the 410 and 670 km seismic discontinuities in the vicinity of the British Isles suggests that this layer is being injected horizontally and is not being vertically fed.

The irregular planform of the Icelandic plume can be used to estimate the number and wavelength of viscous fingers. By ignoring the way in which fingers develop within the non-linear regime, we can use a leading-order planform described by

$$r(t) = r_o + A(t) \cos n\theta \quad (5)$$

where  $r(t)$  is the inscribed present-day planform as a function of time,  $r_o = 500 \text{ km}$  is the radius of the central part of the plume

that probably also varies with time,  $A(t)$  is the present-day finger amplitude as a function of time,  $n$  is the mode (i.e. the number of fingers), and  $\theta$  is the radial angle (Fig. 1b). By identifying and fitting finger tips, we find that  $n$  is  $5 \pm 1$  (see inset of Fig. 4). The average wavelength of the fingers is

$$\lambda = \frac{2\pi r_o}{n} \quad (6)$$

which yields  $\lambda = 628_{524}^{785}$  km. Fingers appear to be best developed beneath oceanic plates and beneath the Phanerozoic lithosphere of the northwest continental shelf of Europe. Thicker lithosphere of the Greenland and Fennoscandian cratons appear to act as bulwarks around which lower viscosity asthenospheric material can flow, suppressing finger development.

Finally, we consider the vigor of the Icelandic plume. Parnell-Turner et al. (2014) use the geometry of the diachronous V-shaped ridges that straddle the Reykjanes Ridge south of Iceland to calculate the mass flux of the plume,  $Q$ . The five youngest pairs of ridges yield a volume flux of  $Q = (1.7 \pm 0.3) \times 10^3 \text{ m}^3 \text{ s}^{-1}$ . This value is equivalent to a buoyancy flux of  $28 \pm 5 \text{ Mg s}^{-1}$  given an asthenospheric mantle density of  $3.2 \text{ Mg m}^{-3}$  and an excess temperature of  $150^\circ\text{C}$ . Significantly, Parnell-Turner et al. (2014) also describe two alternative methods for estimating  $B$  that agree within error with this value. First, the changing boundary between smooth and rough oceanic crust south of Iceland yields  $26 \pm 9 \text{ Mg s}^{-1}$ . Secondly, the present-day planform of the plume swell constrains its excess volume which is maintained by buoyancy flux. For a plume radius of  $1200 \pm 100 \text{ km}$  that grew over the last 30–40 Ma,  $B = 27 \pm 5 \text{ Mg s}^{-1}$  (M. Hoggard, personal communication, 2017).

We note that several popular estimates of the buoyancy flux of the Icelandic plume must be incorrect. Sleep (1990) assumes that the plume flux is given by

$$B = \rho_m \alpha \bar{T} S Y (L + A/2) \quad (7)$$

where  $S$  is full spreading rate (e.g. 16.5 mm/yr),  $L$  and  $A$  are thicknesses of lithosphere and asthenosphere away from ridge taken to be 100 km each, and  $Y$  is along-strike distance supplied by plume. This equation yields a buoyancy flux range of 1.25–1.56  $\text{Mg s}^{-1}$ , which is more than one order of magnitude smaller than the value obtained by Parnell-Turner et al. (2014). There are two serious problems with this analysis. First of all, Sleep (1990) assumes a plume radius of 800 km, even though it is generally agreed that the Icelandic plume has a radius of 1200 km (White, 1997). Secondly, and more crucially, Sleep (1990) assumes that the average velocity within the plume head (i.e. asthenospheric layer) is much slower than the spreading velocity of the lithospheric plates. This assumption is erroneous since we know from the geometry of the V-shaped ridges that the asthenospheric velocity is more than ten times that of plate spreading.

In a second approach, Sleep (1997) assumes that lateral flow of plume material is primarily driven by local buoyancy forces. Sleep (1997) use a simplified analysis of a gravity current to obtain an approximate expression for volume flux where

$$Q = \frac{\delta \rho g W S_{AO}^3 S_{BO}}{Y \eta_p} \quad (8)$$

where  $S_{AO}$  is maximum thickness of plume material at center of rift,  $S_{BO}$  is depth to base of plume material at distal end of rift,  $W$  is width of rift, and  $\eta_p$  is the viscosity of the asthenosphere. If we use Sleep's (1997) values for these parameters combined with the predicted plume spreading shown in his Fig. 7, we find that the buoyancy flux of the Icelandic plume varies dramatically with time. For example, for 0–1 Myrs in his Fig. 7, the buoyancy flux

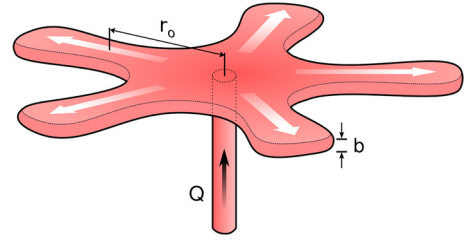


**Fig. 5. Schematic geometry of plume.** Cartoon showing idealized geometry of Icelandic plume. Vertical conduit with radius of  $\sim 100 \text{ km}$  centered beneath Iceland through which hot plume material ascends with volume flux of  $Q$ . This hot material spreads and fingers radially away from Iceland within layer of thickness  $b$ .  $r_o =$  radius of central portion of plume.

is  $50.4 \text{ Mg s}^{-1}$  but between 5 and 10 Myrs, the buoyancy flux decreases to  $0.08 \text{ Mg s}^{-1}$ . This behavior is exactly what is expected for buoyancy spreading of a viscous blob. Spreading of a gravity current probably does not apply to the Icelandic plume for two important reasons. First, the flow of plume material up a conduit into the growing plume head is neglected, which is why plume flux decreases dramatically with time. Secondly, even if the Icelandic plume was not supplied with plume material through a conduit, Sleep's (1997) scheme predicts that the V-shaped ridges should be strongly curved whereas they are almost, but not quite, linear (Ito, 2001).

We can now use our self-consistent estimates of volume flux to determine the cross-gap Péclet number,  $Pe$ , which is the dimensionless ratio of the advective and diffusive transport rates (Rudge et al., 2008). It is given by

$$Pe = \frac{Q}{b\kappa} \quad (9)$$

where  $\kappa = 8 \times 10^{-7} \text{ m}^2 \text{ s}^{-1}$  is the thermal diffusivity of mantle rocks. This equation yields  $Pe = (2.1 \pm 0.4) \times 10^4$  for  $b = 100 \pm 20 \text{ km}$ . This value is large compared to unity and indicates that advection of heat dominates and so the fingering interface is not diffuse.

### 3. Saffman–Taylor instability

When a less viscous fluid displaces a more viscous fluid, the boundary between the two fluids can become unstable and promote viscous fingering (Saffman and Taylor, 1958). A considerable amount of experimental and theoretical work has been carried out on this fingering process for a variety of geometries under different dynamic conditions. The general aim is to predict conditions under which fingering occurs and to estimate the number of fingers that develop (Homsy, 1987). Here, the relevant problem is radial miscible fingering within the horizontal gap of a Hele–Shaw cell (Fig. 5).

Fig. 6 shows planforms of fluid displacement from a series of Hele–Shaw experiments in which radial and miscible viscous fingering is achieved by injecting water into glycerine (Chui, 2012). In these experiments, the mobility ratio,  $M$ , the Péclet number,  $Pe$ , and the aspect ratio (i.e. the ratio of the planform radius,  $r$ , to the layer thickness,  $b$ ) were systematically varied. The number of fingers is controlled by a balance between the Saffman–Taylor instability mechanism and dissipative processes. At low Péclet numbers, diffusion plays the significant stabilizing role. At higher Péclet numbers, diffusion becomes less effective and other mechanisms must fulfill this role. Paterson (1985) proposed that viscous dissipation acts to damp finger growth since the development of fingers increases shearing rates. By arguing that viscous dissipation is minimized, Paterson (1985) showed that the ‘most dangerous’ (i.e. rapidly growing) mode is given by

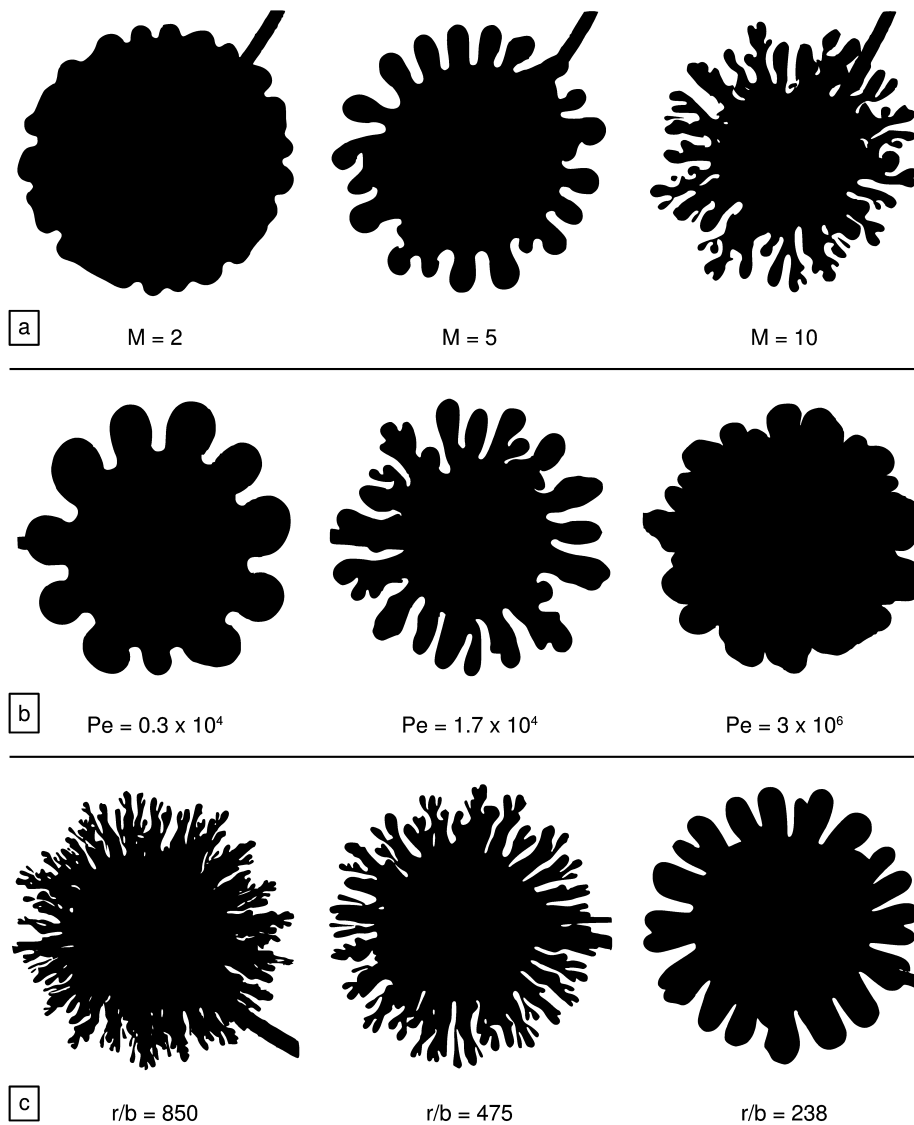


**Fig. 6. Laboratory experiments.** Redrawn, silhouetted images of radial miscible viscous fingering laboratory experiments carried out using different water–glycerol mixtures by [Chui \(2012\)](#). Black splodges = injected water; surrounding white regions = invaded glycerine. (a) Mobility ratios of  $M = 2, 5$  and  $10$ ;  $Pe = 1.7 \times 10^4$ ;  $b = 0.05$  mm; average radius of left-hand panel =  $40$  mm. (b) Cross-gap Péclet numbers of  $Pe = 0.3 \times 10^4, 1.7 \times 10^4$  and  $3 \times 10^6$  for  $M = 10$  calculated from volumetric injection rates, gap thickness,  $b = 0.1$  mm, and diffusion coefficient for water–glycerol mixture,  $\kappa = 10^{-10}$   $\text{m}^2 \text{s}^{-1}$  reported by [Chui \(2012\)](#). (c) Radius-gap thickness ratios,  $r/b = 850, 475$  and  $238$  where  $b = 0.05, 0.1$  and  $0.2$  mm;  $M = 5$ ;  $Pe = 1.7 \times 10^5$ .

$$n = 1 + \left(2 + \frac{5r^2}{2b^2}\right)^{1/2} \quad (10)$$

If the aspect ratio,  $r/b$ , is large then a useful rule of thumb is that the wavelength of the most dangerous mode scales according to  $\lambda \sim 4b$ . [Paterson \(1985\)](#) and [Chui \(2012\)](#) both found that this relationship was consistent with their experimental results. Similarly, [Chen \(1989\)](#) suggested, that at sufficiently high Péclet numbers, the wavelength of fingers is insensitive to the exact value of  $Pe$ . Instead, wavelength scales with the gap width so that  $\lambda/b$  is between 5 and 10. For their experiments on miscible rectilinear flow through a relatively wide gap, [Snyder and Tait \(1998\)](#) argued that  $\lambda/b$  was insensitive to mobility ratio and that  $1 \lesssim \lambda/b \lesssim 3$ . [Chui et al. \(2015\)](#) suggest that there are two regimes for the evolution of the fluid–fluid interface. At early times, interface length increases linearly with time, which is typical of the Saffman–Taylor instability. However, at longer times, interface growth slows and scales as  $t^{1/2}$ , as expected for stable displacement. Their results imply that the instability shuts off and, in this way, the geometry of fingers

becomes fixed. A significant factor may be competition between advective and diffusive time scales at the displacement front itself.

With regard to the Icelandic plume, the most relevant experiments were carried out by [Holloway and de Bruyn \(2005\)](#). In their systematic presentation of Hele–Shaw cell experiments, hot glycerine was injected into cold glycerine for mobility ratios of  $M = 0–90$ , for a range of injection rates that correspond to  $Pe = (1.1–3.5) \times 10^4$ , and for different values of  $b$ . [Holloway and de Bruyn \(2005\)](#) were confident that the fingering they observed was not caused by a thermoviscous instability generated by the proximity of colder walls. They obtained two significant results. First, they showed that the presence or absence of viscous fingering primarily depends upon the values of  $M$  and  $Pe$ . [Fig. 7](#) summarizes their experimental results, enabling fingering and non-fingering fields to be delineated. This field diagram suggests that viscous fingering occurs if  $M \gtrsim 20$  and  $Pe \gtrsim 1.5 \times 10^4$ . Secondly, they corroborated [Paterson’s \(1985\)](#) argument that the wavelength of the fingering instability is proportional to cell width. They found that  $\lambda \sim 5b$  with evidence that the constant of proportionality decreases for increasing values of  $b$ . Their largest value of

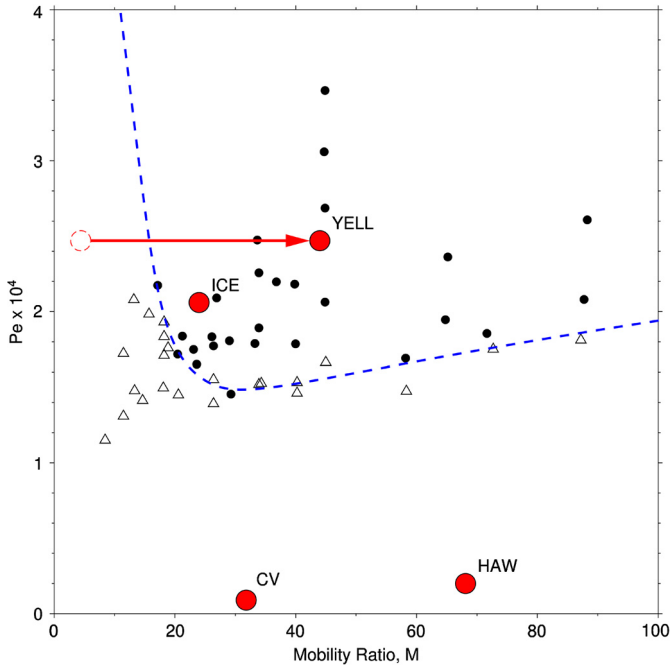


**Fig. 7. Experimental analysis.** Cross-gap Péclet number,  $Pe$ , plotted as function of mobility ratio,  $M$ , for 49 Hele Shaw cell experiments carried out by injecting hot glycerine into cold glycerine with constant plate separation of 1 mm (Holloway and de Bruyn, 2005). Solid circles (open triangles) = experiments for which fingering is (is not) observed; dashed line = demarcation of fingering and no fingering regimes; red circles labeled Ice, Yell, CV and Haw = loci of Icelandic, Yellowstone, Cape Verde and Hawaiian plumes, respectively; red arrow = shift in value of  $M$  when viscosity of plume is decreased by factor of 10. Experimental inlet pressure measurements from Holloway and de Bruyn (2005) converted using  $Pe = \pi \Delta P b^2 / (6\eta\kappa \ln(r_{out}/r_{in}))$ , assuming radial flow according to Darcy's law where  $r_{in} = 0.8$  mm is the radius of inlet nozzle,  $r_{out} = 50$  mm is radius of upper plate,  $b = 1$  mm is cell width,  $\Delta P$  is pressure difference,  $\eta$  is viscosity of defending fluid. For  $M = 20$  on their Fig. 6,  $P = 43.6$  kPa is equivalent to  $Pe = 1.7 \times 10^4$ . Calculated values of  $Pe$  are slight overestimates if pressure drop along capillary tubing is ignored. Ratio of pressure drop along capillary tubing,  $\Delta P_{cap}$ , and pressure drop across cell,  $\Delta P_{cell}$ , is  $\Delta P_{cap} / \Delta P_{cell} = (4Lb^3) / \{3MR^4 \ln(R_{out}/R_{in})\}$  where  $L$  is the length of capillary tubing which must be at least several cm long. If we assume that  $L = 1$  cm,  $\Delta P_{cell} = \Delta P / 1.2$  which reduces  $Pe$  to  $1.4 \times 10^4$ . Note that conversion from  $\Delta P$  to  $Pe$  differs from that of Holloway and de Bruyn (2005) who neglected radial dependence of pressure gradient. For interpretation of colors in this figure, reader is referred to web version of this article.

$b$  yields an aspect ratio comparable to that observed for the Icelandic plume (i.e.  $\sim 12$ ; their Fig. 3c).

When the gap thickness,  $b$ , is large, the buoyancy contrast between the invading and defending fluids probably plays a significant role. This contrast introduces hydrostatic pressure gradients that cause the flow to resemble a gravity current between confining surfaces rather than horizontal flow within a classical Hele-Shaw cell (Snyder and Tait, 1998). The importance of such hydrostatic pressure gradients relative to those that drive the flow can be gauged by considering a gravity number given by

$$G = \frac{2\pi r_o b^3 g \Delta \rho}{\eta Q} \quad (11)$$

where  $\Delta \rho$  is the density contrast between invading and defending fluids (Greenkorn et al., 1967; Chui, 2012). For the Icelandic plume where  $\eta \sim 10^{19}$  Pa s and  $\Delta \rho = \alpha(T - T_r)\rho_m$ ,  $G \approx 30$ , which suggests that buoyancy does play a role in a complete dynamical analysis of radial viscous fingering. Significantly, Snyder and Tait's (1998) experimental results imply that even when buoyancy contrasts are large, the wavelength of fingering scales with  $b$ . In this case, radial spreading occurs by a gravity-driven current which may cause the growth of higher modes to be strongly damped.

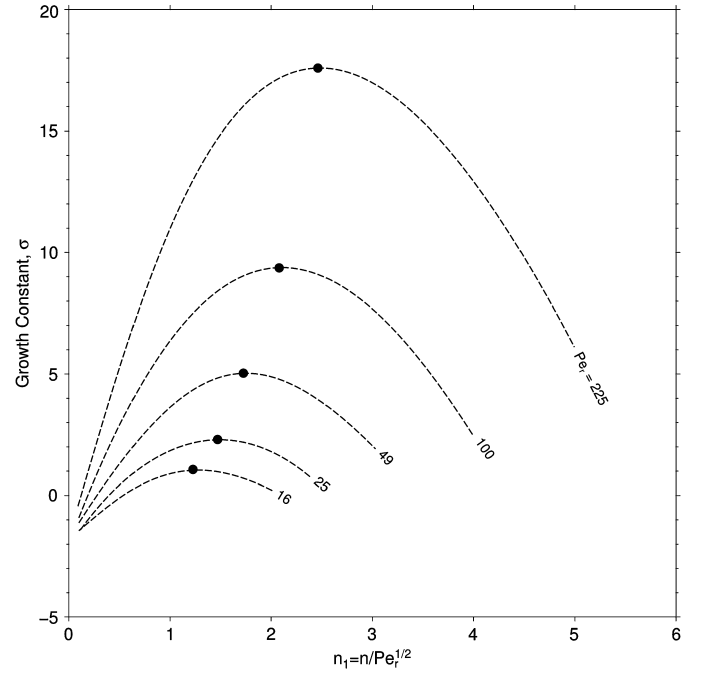


**Fig. 8. Linear stability analysis.** Growth of fingering modes as function of wavenumber for range of radial Péclet numbers (redrawn from Fig. 2 of Tan and Homsy, 1987). Solid circles = most dangerous modes.

Finally, we note that a considerable body of theoretical analysis has been carried out on radial miscible fingering which generally assumes Darcy flow through a porous medium. If the aspect ratio of radial flow is large and if the wavelengths of interest are much greater than  $b$ , this analogy holds and the problem can be attacked using linear perturbation analysis (e.g. Tan and Homsy, 1987). Significantly, growth of perturbation for radial source flow is principally controlled by  $M$  and by the radial Péclet number,  $Pe_r = Q/r_o\kappa$ , rather than the cross-gap Péclet number (Fig. 8). For  $M = 20$ – $150$ , it has been shown that the eigenvalue which determines the growth of perturbations,  $\sigma$ , is negative for all modes (i.e. no growth of perturbations), provided that  $Pe_r$  is small.  $\sigma$  increases with  $Pe_r$  and changes sign for modes of  $n \geq 3$  when  $Pe_r \sim 10$ . For larger values of  $Pe_r$ , perturbation analysis demonstrates that there is always both a cut-off and a most dangerous mode. The value of the most dangerous mode and the number of unstable modes increase with  $Pe_r$ . For asymptotically large values of  $Pe_r$ , Tan and Homsy (1987) showed that

$$\sigma = \frac{\log M \sqrt{Pe_r}}{\sqrt{\pi}} \left\{ 1 - \frac{\sqrt{Pe_r}}{n} \right\} - \frac{n^2}{Pe_r}. \quad (12)$$

In this case, the most dangerous mode is given by

$$n_{max} = (\log M / 2\sqrt{\pi})^{1/3} Pe_r^{2/3}. \quad (13)$$

For large values of  $Pe_r$ , the predicted wavelengths rapidly decrease and the assumption of Darcy flow inevitably breaks down. Instead, it is necessary to have recourse, as we have done, to a combination of experimental analyses and heuristic arguments.

#### 4. Discussion

Fig. 5 captures the idealized geometry of the Icelandic plume. On Iceland itself, the putative conduit is located at Vatnajökull in southeast Iceland and has a diameter of  $\sim 100$  km (Fig. 1; Shorttle et al., 2010). We have shown that  $M = 24 \pm 10$ ,  $Pe = (2.1 \pm 0.4) \times 10^4$  and  $b = 100 \pm 20$  km for the Icelandic plume. By combining this scaling analysis with the results of laboratory experiments on



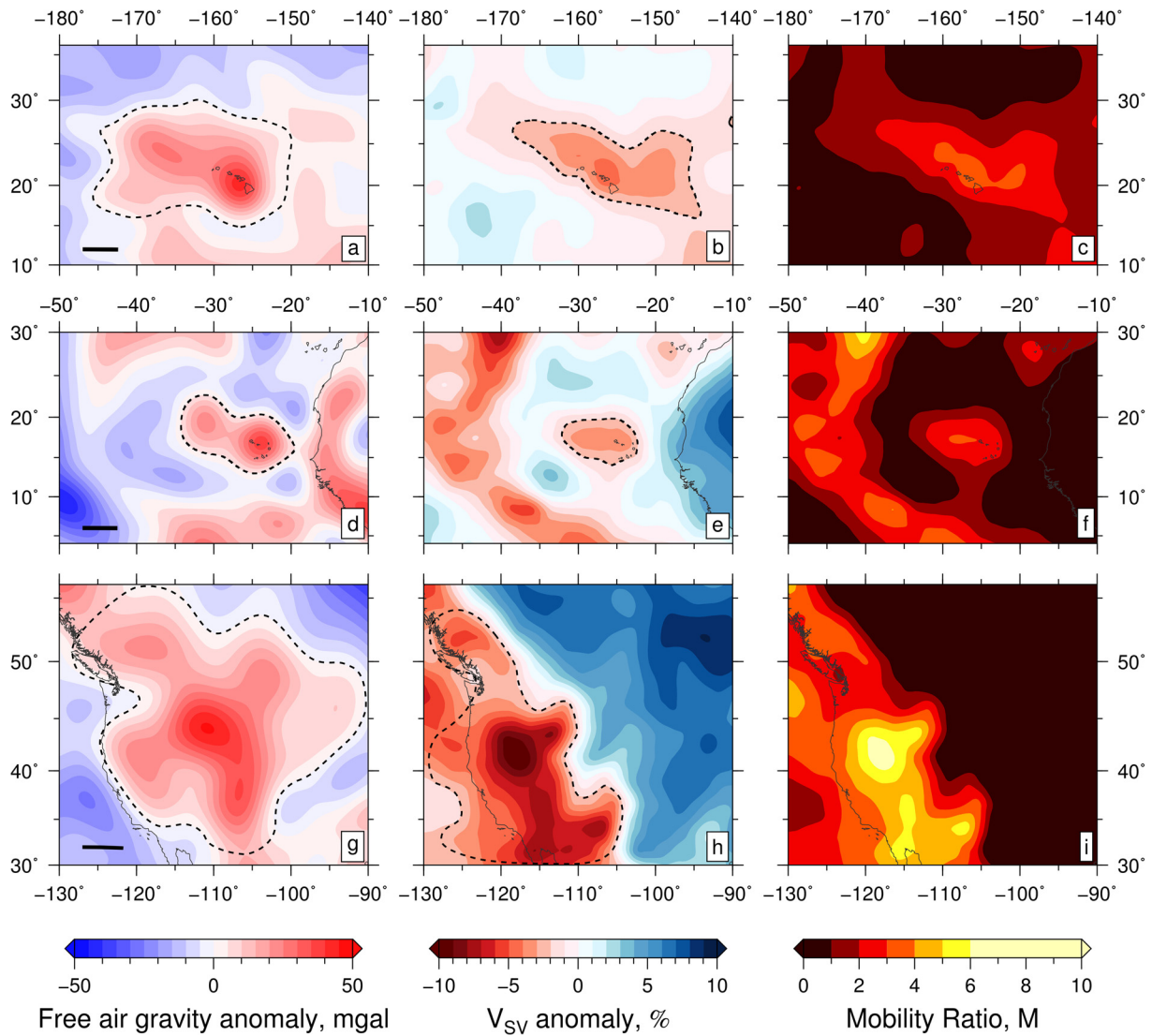


**Fig. 9. Plume planforms and mobility ratios.** (a) Long wavelength (700–2500 km) free-air gravity anomaly centered on Hawaiian plume. Dashed line = locus of zero contour except along southern edge; black bar = 500 km. (b) Shear wave velocity anomaly at depth of 100 km (Schaeffer and Lebedev, 2013). Dashed line = approximate extent of anomaly. (c) Mobility ratio,  $M$ , calculated by converting shear wave velocity anomaly into temperature and viscosity according to Equations (2)–(4). (d)–(f) Cape Verde plume. (g)–(i) Yellowstone plume.

radial miscible viscous fingering, we suggest that a Saffman–Taylor instability will manifest itself at the distal fringes of the Icelandic plume (Fig. 7). Since the Icelandic plume fluctuates through time, we expect that these radial fingers wax and wane, giving rise to complex spatial and temporal patterns of epeirogeny.

It is helpful to place this result in context by considering three other well-known plumes (see Table 1). We start with the Hawaiian plume which is well studied and is often compared with the Icelandic plume. This plume has a smaller planform and a smaller melt production rate, both of which suggest that its buoyancy flux is also smaller (Fig. 9a). Sleep (1990) suggested that the Hawaiian plume has a buoyancy flux of  $8.7 \text{ Mg s}^{-1}$ . A combination of basaltic geochemistry and numerical convective modeling was used by Watson and McKenzie (1991) to calculate the detailed thermal structure of this plume. They argued that the core of the Hawaiian plume has a potential temperature of  $1558^\circ\text{C}$ , a viscosity of  $\eta = 10^{16} \text{ Pa s}$ , and a bathymetric swell with a maximum amplitude of about 1.3 km extending over a radius of  $r > 500 \text{ km}$ . Ribe and Christensen (1999) analyze the dynamic evolution of the Hawaiian plume beneath a moving plate by carrying out a series of

three-dimensional convective simulations with temperature- and depth-dependent viscosity. They incorporated a melting parameterization together with the effects of depletion buoyancy and obtained  $B = 2.2\text{--}3.5 \text{ Mg s}^{-1}$  and  $\eta = 8 \times 10^{17} \text{ Pa s}$  for a temperature anomaly of  $293^\circ\text{C}$  and an observed plume swell radius of  $r = 600 \pm 50 \text{ km}$ . Finally, Crosby and McKenzie (2009) estimate a buoyancy flux of  $6\text{--}8 \text{ Mg s}^{-1}$  and a melt production rate of  $3\text{--}4 \text{ m}^3 \text{ s}^{-1}$ . Based upon these largely consistent results, we assume that the Hawaiian plume has a buoyancy flux of  $B = 5 \text{ Mg s}^{-1}$  and an excess temperature of  $250^\circ\text{C}$ . We use a layer thickness of  $b = 120 \text{ km}$  in agreement with seismologic constraints. These values yield  $Pe = 0.2 \times 10^4$  and  $M = 68$  which suggest that the planform of the Hawaiian plume is not expected to have developed radial viscous fingering, in accordance with independent observations (Figs. 7 and 9a–c).

Arachchige (2016) carried out radial viscous fingering experiments with a moving surface boundary that suggest that fingers could be significantly deformed, and even obliterated, if plate velocity is significant. One way of testing this possibility is to compare the Hawaiian plume with a plume of similar size and vigor



which lies beneath a slow-moving plate. Here, we have chosen to analyze the Cape Verde plume. This plume has a maximum amplitude of  $1900 \pm 200$  m and a swell radius of  $r = 390 \pm 20$  km (Courtney and White, 1986; Fig. 9d). Although it is less well studied than the Hawaiian plume, Holm et al. (2006) exploited inverse modeling of trace elements to calculate a temperature anomaly of  $190^\circ\text{C}$ . Crosby and McKenzie (2009) estimate a buoyancy flux of  $B = 0.7 \text{ Mgs}^{-1}$  which is consistent with a layer thickness of 80–90 km and a thermal time constant of 30 Ma. Here, we suggest that the planform of the Cape Verde plume is consistent with  $B = 2 \text{ Mgs}^{-1}$ . We assume a temperature anomaly of  $190^\circ\text{C}$  and  $b = 130$  km. These values yield  $Pe = 0.09 \times 10^4$  and  $M = 31$  which imply that a viscous fingering instability should not be expected (Fig. 9d–f). This result suggests that the absence of a viscous fingering instability for the Hawaiian plume is not necessarily a consequence of the fast velocity of the overlying lithosphere (Arachchige, 2016).

Finally, and more controversially, we consider the Yellowstone plume which is characterized by regional elevation, anomalous heatflow, an irregular-shaped long wavelength free-air gravity anomaly, and voluminous basaltic volcanism (Fig. 9g–i). Although the Yellowstone plume *sensu stricto* is situated at the northeastern end of a short volcanic track, shear wave velocity anomalies are distributed over a much wider area that is consistent with the regional extent of elevated topography and of basaltic volcanism. Schutt and Dueker (2008) suggest that extremely low shear wave velocities beneath the plume of  $3.8 \pm 0.1$  km/s are consistent with temperature anomalies of  $55\text{--}80^\circ\text{C}$ . Although Smith et al. (2009) argue that the Yellowstone plume is cool and weak with a small buoyancy flux of  $B = 0.25 \text{ Mgs}^{-1}$ , the extent and amplitude of the topographic swell and of the long wavelength free-air gravity anomalies imply that  $B$  is greater (Fig. 9g). A conservative estimate of  $B$  can be made by first converting the pattern of free-air gravity anomalies into dynamic topography using an observed admittance of  $15 \text{ mGal km}^{-1}$  at wavelengths of greater than 1000 km. This conversion yields an excess volume of  $\sim 5 \times 10^6 \text{ km}^3$ . For a time constant of 30 Ma and an asthenospheric density of  $\rho_m = 3.2 \text{ Mg m}^{-3}$ , we obtain a buoyancy flux of  $B = 17 \text{ Mgs}^{-1}$ . If the average temperature anomaly is  $80^\circ\text{C}$  and if  $b = 100$  km, we obtain  $Pe = 2.4 \times 10^4$  and  $M = 4.4$  which suggest that viscous fingering should not occur (Fig. 7).

This result is surprising because both the planform of the long wavelength free-air gravity and the spatial distribution of shear wave velocity anomalies suggest that there are as many as four prominent fingers (Obrebski et al., 2011). One possibility is that the viscosity of this plume is lower than expected because of the proximity of the subducting Farallon slab during the early stages of plume development. The Cenozoic history of basaltic volcanism throughout western North America shows that there is a dramatic transition from enriched basalts to ocean island basalts at  $\sim 5$  Ma. There is strong evidence that asthenospheric melting is influenced in significant ways by hydrous melt fractions. These fractions will have a dramatic effect on asthenospheric viscosity which means that the value of  $M$  may be considerably underestimated if it is calculated from temperature alone using Equations (2)–(4). Hirth and Kohlstedt (2003) argue that water content of the mantle wedge adjacent to subduction zones can cause the viscosity of olivine aggregates to decrease exponentially with increasing melt content. They suggest that viscosity could be lowered by one order of magnitude. This suggestion is supported by the calculations of McCarthy and Takei (2011) and Holtzman (2016) which show that the presence of a melt fraction as low as 0.01 can reduce viscosity by up to several orders of magnitude. Here, we assume that viscosity is reduced ten fold which increases  $M$  from 4.4 to 44 and shifts the Yellowstone plume into the field where viscous fingering is expected.

**Table 1**  
Parameter values for plumes.

Plume	Radius (km)	$\Delta T$ ( $^\circ\text{C}$ )	$B$ ( $\text{Mgs}^{-1}$ )	$b$ (km)	$M$	$Pe \times 10^4$
Iceland	1200	150	27	100	24	2.06
Hawaii	500	250	5	120	68	0.20
Cape Verde	390	190	2	130	31	0.09
Yellowstone	1000	80	17	100	4.4	2.44

## 5. Conclusions

We use a combination of geophysical and geologic observations from the North Atlantic Ocean to confirm that the Icelandic plume has an irregular planform. Sub-plate and physiographic evidence shows that about five radial fingers of hot asthenosphere protrude beneath adjacent continental margins. A quantitative comparison with appropriately scaled laboratory experiments suggests that these fingers are generated by the classic Saffman–Taylor instability. This manifestation of viscous fingering within rapidly outward-flowing asthenosphere has significant implications for the spatial and temporal evolution of convectively maintained topography (Morgan et al., 2013). For example, an alternating pattern of rapid Neogene uplift and subsidence occurs across the northwest European shelf from west of Ireland to Scandinavia (Anell et al., 2009). This pattern matches the configuration of sub-plate fingering and suggests that shallow, small-scale convective circulation can generate and maintain surface deformation on relatively short length scales. The temporal evolution of this circulation has significant consequences for regional exhumation, for deposition of clastic sediments, for halokinesis in the southern North Sea, and for source rock maturation. It also helps to account for the development of youthful penneplains whose age and origin are much debated. Finally, a rapidly evolving and irregular plume planform appears to have had a significant influence in moderating the overflow of North Atlantic Deep Water and its ancient precursor (Poore et al., 2011).

In contrast, the planforms of smaller convective upwellings such as the Hawaiian and Cape Verde plumes have regular planforms that do not exhibit a radial fingering instability. We suggest that an absence of fingering is principally a consequence of smaller buoyancy fluxes. More speculatively, we propose that the Yellowstone plume *sensu lato* exhibits long wavelength radial fingering. Since this plume has an excess asthenospheric temperature of not more than  $55\text{--}80^\circ\text{C}$ , it is necessary to invoke a one order of magnitude reduction in plume-head viscosity which may arise from the presence of minor fractions of hydrous melt.

For symbols notation see Table 2.

## Correspondence

Correspondence and requests for materials should be addressed to N.J. White.

## Author contributions

This project was conceived and managed by NJW. CMS processed data with guidance from NJW. DP provided mathematical analysis and insight in consultation with NJW. The paper was written by NJW with contributions from CMS and DP.

## Competing financial interests

The authors declare no competing financial interests.

**Table 2**  
Notation.

Symbol	Quantity	Units	Value
$b$	Thickness of gap and asthenospheric layer	km	
$U$	Surface uplift	km	
$r$	Radius of present-day plume planform	km	
$r_o$	Radius of central part of plume	km	500
$A(t)$	finger amplitude at time $t$	km	
$\lambda$	Radial wavelength	km	
$L$	Lithospheric thickness	km	100
$A$	Asthenospheric thickness	km	100
$Y$	Along strike distance supplied by plume	km	
$W$	Width of rift	km	
$S$	Full spreading rate	mm yr <sup>-1</sup>	16.5
$S_{AO}$	Central maximum plume thickness	km	
$S_{BO}$	Distal plume thickness	km	
$V_s$	Shear wave velocity	km s <sup>-1</sup>	
$\theta$	Radial angle	rad	
$n$	Number of fingers (i.e. mode)	–	
$n_{max}$	Most dangerous mode	–	
$T_r$	Ambient asthenospheric temperature	°C	1315
$\bar{T}$	Average excess temperature	°C	
$T$	Temperature of invading fluid	°C	
$\alpha$	Thermal expansivity	°C <sup>-1</sup>	$3.4 \times 10^{-5}$
$\kappa$	Thermal diffusivity	m <sup>2</sup> s <sup>-1</sup>	$8 \times 10^{-7}$
$g$	Gravitational acceleration	m s <sup>-2</sup>	9.81
$\eta$	Viscosity of invading fluid	Pa s	
$\eta_r$	Viscosity of defending fluid	Pa s	
$\eta_p$	Viscosity of asthenosphere	Pa s	
$M$	Mobility	–	
$Pe$	Cross-gap Péclet number	–	
$Pe_r$	Radial Péclet number	–	
$G$	Gravity number	–	
$Q$	Volume flux	m <sup>3</sup> s <sup>-1</sup>	
$B$	Buoyancy flux	Mg s <sup>-1</sup>	
$\rho_m$	Asthenospheric mantle density	Mg m <sup>-3</sup>	3.2
$\Delta\rho$	Density contrast between invading and defending fluid	Mg m <sup>-3</sup>	
$Z$	Water-loaded admittance	mGal km <sup>-1</sup>	25
$R$	Gas constant	J mol <sup>-1</sup> K <sup>-1</sup>	8.3
$E$	Activation energy of mantle rock	kJ mol <sup>-1</sup>	409 ± 50

## Acknowledgements

CMS is supported by Shell Exploration and by the British Geological Survey. We thank M. Hoggard, C. Richardson, and A. Woods for their help. M. Ballmer provided a constructive review. This paper is dedicated to Maeve White. Figures were prepared using Generic Mapping Tools. Cambridge Earth Sciences contribution number esc. 3904.

## References

- Anell, I., Thybo, H., Artemieva, I.M., 2009. Cenozoic uplift and subsidence in the North Atlantic region: geological evidence revisited. *Tectonophysics* 474, 78–105. <http://dx.doi.org/10.1016/j.tecto.2009.04.006>.
- Arachchige, U.S.N., 2016. Formation of Intraplate Seamount Chains by Viscous Fingering Instabilities in the Asthenosphere Using Low Reynolds Number Miscible Fluids with a Moving Surface Boundary. Unpublished MSc Dissertation, California State University, Northridge, USA.
- Ballmer, M.D., Conrad, C.P., Smith, E.I., Harmon, N., 2013. Non-hotspot volcano chains produced by migration of shear-driven upwelling toward the East Pacific Rise. *Geology* 41, 479–482. <http://dx.doi.org/10.1130/G33804.1>.
- Behn, M.D., Hirth, G., Elsenbeck II, J.R., 2009. Implications of grain size evolution on the seismic structure of the oceanic upper mantle. *Earth Planet. Sci. Lett.* 282, 178–189. <http://dx.doi.org/10.1016/j.epsl.2009.03.014>.
- Bijwaard, H., Spakman, W., 1999. Tomographic evidence for a narrow whole mantle plume below Iceland. *Earth Planet. Sci. Lett.* 166, 121–126. [http://dx.doi.org/10.1016/S0012-821X\(99\)00004-7](http://dx.doi.org/10.1016/S0012-821X(99)00004-7).
- Bott, M.H.P., Bott, J.D.J., 2004. The Cenozoic uplift and earthquake belt of mainland Britain as a response to an underlying hot, low-density upper mantle. *J. Geol. Soc.* 161, 19–29. <http://dx.doi.org/10.1144/0016-764903-014>.
- Chen, J.D., 1989. Growth of radial viscous fingers in a Hele–Shaw cell. *J. Fluid Mech.* 201, 223–242. <http://dx.doi.org/10.1017/S00222112089000911>.
- Chui, J., 2012. Understanding the Evolution of Miscible Viscous Fingering Patterns. Unpublished MSc Dissertation, Massachusetts Institute of Technology, Cambridge, USA.
- Chui, J.Y.Y., de Anna, P., Juanes, R., 2015. Interface evolution during radial miscible viscous fingering. *Phys. Rev. E* 92, 041003. <http://dx.doi.org/10.1103/PhysRevE.92.041003>.
- Courtney, R.C., White, R.S., 1986. Anomalous heat flow and geoid across the Cape Verde Rise: evidence for dynamic support from a thermal plume in the mantle. *Geophys. J. R. Astron. Soc.* 87, 815–867. <http://dx.doi.org/10.1111/j.1365-246X.1986.tb01973.x>.
- Crosby, A.G., McKenzie, D., 2009. An analysis of young ocean depth, gravity and global residual topography. *Geophys. J. Int.* 178, 1198–1219. <http://dx.doi.org/10.1111/j.1365-246X.2009.04224.x>.
- Davis, M.W., White, N.J., Priestley, K.F., Baptie, B.J., Tilmann, F.J., 2012. Crustal structure of the British Isles and its epeirogenic consequences. *Geophys. J. Int.* 190, 705–725. <http://dx.doi.org/10.1111/j.1365-246X.2012.05485.x>.
- Greenkorn, R.A., Matar, J.E., Smith, R.C., 1967. Two-phase flow in Hele–Shaw models. *AIChE J.* 13, 273–279. <http://dx.doi.org/10.1002/aic.690130217>.
- Harmon, N., Forsyth, D.W., Weeraratne, D.S., Yang, Y., Webb, S.C., 2011. Mantle heterogeneity and off axis volcanism on young Pacific lithosphere. *Earth Planet. Sci. Lett.* 311, 306–315. <http://dx.doi.org/10.1016/j.epsl.2011.09.038>.
- Hirth, G., Kohlstedt, D., 2003. Rheology of the Upper Mantle and the Mantle Wedge: A View from the Experimentalists. *American Geophysical Union Geophysical Monograph Series*, vol. 138, pp. 83–105.
- Hoggard, M.J., Winterbourne, J., Czarnota, K., White, N., 2017. Oceanic residual depth measurements, the plate cooling model, and global dynamic topography. *J. Geophys. Res., Solid Earth*. <http://dx.doi.org/10.1002/2016JB013457>.
- Holloway, K.E., de Bruyn, J.R., 2005. Viscous fingering with a single fluid. *Can. J. Phys.* 83, 551–564. <http://dx.doi.org/10.1139/p05-024>.
- Holm, P.M., Wilson, J.R., Christensen, B.P., Hansen, L., Hansen, S.L., Hein, K.M., Mortensen, A.K., Pedersen, R., Plesner, S., Runge, M.K., 2006. Sampling the Cape Verde mantle plume: evolution of melt compositions on Santo Antão, Cape Verde Islands. *J. Petrol.* 47, 145–189. <http://dx.doi.org/10.1093/ptrology/egi071>.
- Holtzman, B.K., 2016. Questions on the existence, persistence, and mechanical effects of a very small melt fraction in the asthenosphere. *Geochem. Geophys. Geosyst.* 17, 470–484. <http://dx.doi.org/10.1002/2015GC006102>.
- Homsy, G.M., 1987. Viscous fingering in porous media. *Annu. Rev. Fluid Mech.* 19, 271–311. <http://dx.doi.org/10.1146/annurev.fl.19.010187.001415>.
- Ito, G., 2001. Reykjanes “V”-shaped ridges originating from a pulsing and dehydrating mantle plume. *Nature* 411, 681–684. <http://dx.doi.org/10.1038/35079561>.

- Jones, S.M., Lovell, B., Crosby, A.G., 2012. Comparison of modern and geological observations of dynamic support from mantle convection. *J. Geol. Soc.* 169, 745–758. <http://dx.doi.org/10.1144/jgs2011-118>.
- Kooi, H., Hettema, M., Cloetingh, S., 1991. Lithospheric dynamics and the rapid Pliocene-Quaternary subsidence phase in the southern North Sea basin. *Tectonophysics* 192, 245–259. [http://dx.doi.org/10.1016/0040-1951\(91\)90102-X](http://dx.doi.org/10.1016/0040-1951(91)90102-X).
- Marquart, G., Schmeling, H., 2004. A dynamic model for the Iceland Plume and the North Atlantic based on tomography and gravity data. *Geophys. J. Int.* 159, 40–52. <http://dx.doi.org/10.1111/j.1365-246X.2004.02398.x>.
- Matthews, S., Shorttle, O., MacLennan, J., 2016. The temperature of the Icelandic mantle from olivine-spinel aluminum exchange thermometry. *Geochem. Geophys. Geosyst.* 17, 4725–4752. <http://dx.doi.org/10.1002/2016GC006497>.
- McCarthy, C., Takei, Y., 2011. Anelasticity and viscosity of partially molten rock analogue: toward seismic detection of small quantities of melt. *Geophys. Res. Lett.* 38, L18306. <http://dx.doi.org/10.1029/2011GL048776>.
- Morgan, J.P., Hasenclever, J., Shi, C., 2013. New observational and experimental evidence for a plume-fed asthenosphere boundary layer in mantle convection. *Earth Planet. Sci. Lett.* 366, 99–111. <http://dx.doi.org/10.1016/j.epsl.2013.02.001>.
- Obrebski, M., Allen, R.M., Pollitz, F., Hung, S.H., 2011. Lithosphere–asthenosphere interaction beneath the western United States from the joint inversion of body-wave traveltimes and surface-wave phase velocities. *Geophys. J. Int.* 185, 1003–1021. <http://dx.doi.org/10.1111/j.1365-246X.2011.04990.x>.
- Parnell-Turner, R., White, N., Henstock, T., Murton, B., MacLennan, J., Jones, S.M., 2014. A continuous 55-million-year record of transient mantle plume activity beneath Iceland. *Nat. Geosci.* 7, 914–919. <http://dx.doi.org/10.1038/ngeo2281>.
- Paterson, L., 1985. Fingering with miscible fluids in a Hele–Shaw cell. *Phys. Fluids* (1958–1988) 28, 26–30. <http://dx.doi.org/10.1063/1.865195>.
- Poore, H., White, N., MacLennan, J., 2011. Ocean circulation and mantle melting controlled by radial flow of hot pulses in the Iceland plume. *Nat. Geosci.* 4, 558–561. <http://dx.doi.org/10.1038/ngeo1161>.
- Priestley, K., McKenzie, D., 2006. The thermal structure of the lithosphere from shear wave velocities. *Earth Planet. Sci. Lett.* 244, 285–301. <http://dx.doi.org/10.1016/j.epsl.2006.01.008>.
- Ribe, N.M., Christensen, U.R., 1999. The dynamical origin of Hawaiian volcanism. *Earth Planet. Sci. Lett.* 171, 517–531. [http://dx.doi.org/10.1016/S0012-821X\(99\)00179-X](http://dx.doi.org/10.1016/S0012-821X(99)00179-X).
- Rickers, F., Fichtner, A., Trampert, J., 2013. The Iceland–Jan Mayen plume system and its impact on mantle dynamics in the North Atlantic region: evidence from full-waveform inversion. *Earth Planet. Sci. Lett.* 367, 39–51. <http://dx.doi.org/10.1016/j.epsl.2013.02.022>.
- Ritsema, J., Deuss, A., van Heijst, H.J., Woodhouse, J.H., 2011. S4ORTS: a degree–40 shear-velocity model for the mantle from new Rayleigh wave dispersion, teleseismic traveltimes and normal-mode splitting function measurements. *Geophys. J. Int.* 184, 1223–1236. <http://dx.doi.org/10.1111/j.1365-246X.2010.04884.x>.
- Rudge, J.F., Shaw Champion, M.E., White, N., McKenzie, D., Lovell, B., 2008. A plume model of transient diachronous uplift at the Earth's surface. *Earth Planet. Sci. Lett.* 267, 146–160. <http://dx.doi.org/10.1016/j.epsl.2007.11.040>.
- Saffman, P.G., Taylor, G., 1958. The penetration of a fluid into a porous medium or Hele–Shaw cell containing a more viscous liquid. *Proc. R. Soc. Lond., Ser. A, Math. Phys. Eng. Sci.* 245, 312–329. <http://dx.doi.org/10.1098/rspa.1958.0085>.
- Schaeffer, A.J., Lebedev, S., 2013. Global shear speed structure of the upper mantle and transition zone. *Geophys. J. Int.* 194, 417–449. <http://dx.doi.org/10.1093/gji/ggt095>.
- Schutt, D.L., Dueker, K., 2008. Temperature of the plume layer beneath the Yellowstone hotspot. *Geology* 36, 623–626. <http://dx.doi.org/10.1130/G24809A.1>.
- Shorttle, O., MacLennan, J., Jones, S.M., 2010. Control of the symmetry of plume-ridge interaction by spreading ridge geometry. *Geochem. Geophys. Geosyst.* 11, Q0AC05. <http://dx.doi.org/10.1029/2009GC002986>.
- Sleep, N.H., 1990. Hotspots and mantle plumes: some phenomenology. *J. Geophys. Res., Solid Earth* 95, 6715–6736. <http://dx.doi.org/10.1029/JB095iB05p06715>.
- Sleep, N.H., 1997. Lateral flow and ponding of starting plume material. *J. Geophys. Res., Solid Earth* 102, 10001–10012. <http://dx.doi.org/10.1029/97JB00551>.
- Smith, R.B., Jordan, M., Steinberger, B., Puskas, C.M., Farrell, J., Waite, G.P., Husen, S., Chang, W.L., O'Connell, R., 2009. Geodynamics of the Yellowstone hotspot and mantle plume: seismic and GPS imaging, kinematics, and mantle flow. *J. Volcanol. Geotherm. Res.* 188, 26–56. <http://dx.doi.org/10.1016/j.jvolgeores.2009.08.020>.
- Snyder, D., Tait, S., 1998. A flow-front instability in viscous gravity currents. *J. Fluid Mech.* 369, 1–21.
- Tan, C.T., Homsy, G.M., 1987. Stability of miscible displacements in porous media: radial source flow. *Phys. Fluids* (1958–1988) 30, 1239–1245. <http://dx.doi.org/10.1063/1.866289>.
- Watson, S., McKenzie, D., 1991. Melt generation by plumes: a study of Hawaiian volcanism. *J. Petrol.* 32, 501–537. <http://dx.doi.org/10.1093/petrology/32.3.501>.
- Weeraratne, D.S., Forsyth, D.W., Yang, Y., Webb, S.C., 2007. Rayleigh wave tomography beneath intraplate volcanic ridges in the South Pacific. *J. Geophys. Res., Solid Earth* (1978–2012) 112. <http://dx.doi.org/10.1029/2006JB004403>.
- Weeraratne, D.S., Parmentier, E.M., Forsyth, D.W., 2003. Viscous fingering of miscible fluids in laboratory experiments and the oceanic mantle asthenosphere. In: *AGU Fall Meeting, AGU, San Francisco, USA*. Abstract no. V21B-03.
- White, R.S., 1997. Rift-plume interaction in the North Atlantic. *Philos. Trans. R. Soc. Lond. A, Math. Phys. Eng. Sci.* 355, 319–339. <http://dx.doi.org/10.1098/rsta.1997.0011>.
- White, R., McKenzie, D., 1989. Magmatism at rift zones: the generation of volcanic continental margins and flood basalts. *J. Geophys. Res.* 94, 7685. <http://dx.doi.org/10.1029/JB094iB06p07685>.